Euler-Bernoulli Theory Accurately Predicts Atomic Force Microscope Shape During Non-Equilibrium Snap to Contact Motion

Thesis Submitted in Partial Fulfillment of
the Jay and Jeanie Schottenstein Honors Program

David Friedenberg

Yeshiva College, Department of Physics
Under the supervision of Dr. Fredy Zypman, Physics
Yeshiva University
May 2020

Contents

1 Introduction

First invented by IBM scientists in 1985, the *Atomic Force Microscope* (AFM) is a device capable of generating nanometer-scale topological and spectroscopic information about a biological or physical sample, even one submerged in a fluid. The unique aspect of the AFM is that it does not use any lenses or beam irradiation (e.g. Electron Microscope), thus it does not suffer limitations in spatial resolution due to diffraction effects. When it was first created, the AFM had a lateral resolution of 30 Å for periodically arranged structures such as carbon-based materials, and has a general lateral resolution of 1000 Å and a vertical resolution of 1 Å for most materials, which is even less than the length of a single atom [1]. This is almost 1000 times better resolution than the optical diffraction limit for visible light, allowing researchers to study materials with a higher level of accuracy without compromising the sample with high energy X-ray radiation.

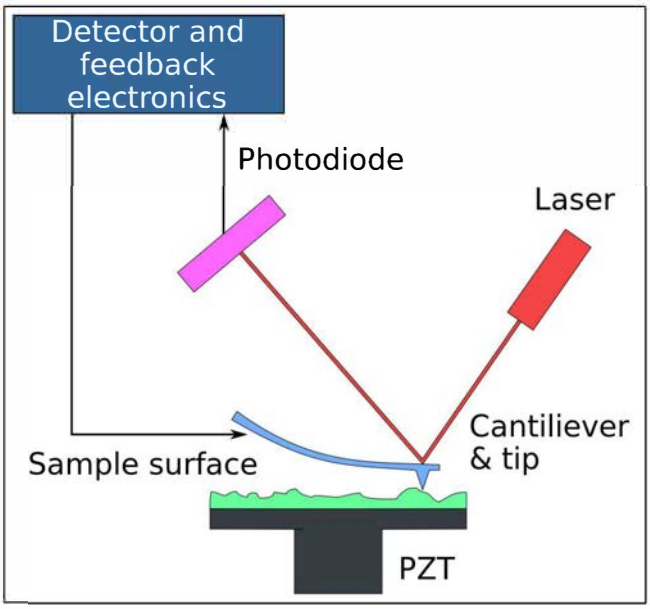

Figure 1: The basic apparatus of an AFM. The tip on the free end of the cantilever is brought near to the sample, thus changing the location which the laser light hits the photodiode, allowing for indirect measurement of the cantilever vertical deflection. (Public Domain Image)

The way that an AFM measures a sample is analogous to the pickup stylus on a record player. A small (a few micrometers long) flexible rod, known as a *cantilever*, is fixed to a rigid base at one end with a needle tip attached to the free end. This tip is extremely sharp with a radius to the order of a few nanometers

at its apex. As the cantilever is brought near a sample, various forces are acting between the surface of the sample and the tip of the cantilever. Since it is fixed at one end, the cantilever will be bent by these attractive forces. By measuring this bending, one can obtain not only an idea of the relative heights in the sample (topographical information), but can possibly even derive the strength of the forces acting on the cantilever (force spectroscopy). This bending is measured by covering the free end of the cantilever with a reflective coating, and reflecting a laser off the tip onto a distant photodiode detector. By calibrating the photodetector with the cantilever in static equilibrium, the deflection of the cantilever, specifically the slope, can be measured by the vertical motion of the reflected laser onto the photodetector and thus the recorded output voltage. This process is demonstrated in Figure 1.

This measurement process with the AFM is extremely adept at obtaining surface topographical information about a sample and is commonly used in 3-dimensional nanoscale imaging of synthetic and even biological materials. This imaging is done using a process known as a *raster scan*. The AFM cantilever is brought into contact with the sample at a certain location and then "dragged" across the surface of the material. An internal feedback loop is established between the photodetector - which measures the slope of cantilever deflection, and the piezomotors controlling the stage which the sample lies on. As the cantilever moves across the samples surface, the piezomotors are precisely adjusted to allow it to smoothly drag across a row of the sample and simultaneously measure the deflections occurring during this motion. When this process is repeated for various rows along a sample, they can be combined to obtain a full 3D topographical image of the sample of study, thus allowing for a complete analysis of the geometry of a sample. An example of the results of this method of imaging are shown in Figure 2.

Another common use of the AFM is force spectroscopy, or measuring the attractive forces on the surface of a sample. Note that this is very different from the topographical analysis, since studying the forces requires a quantitative analysis of the output voltage from the photodetector rather than just a qualitative study of the relative change across the surface of the sample. This suggests the obvious problem: what is the physical

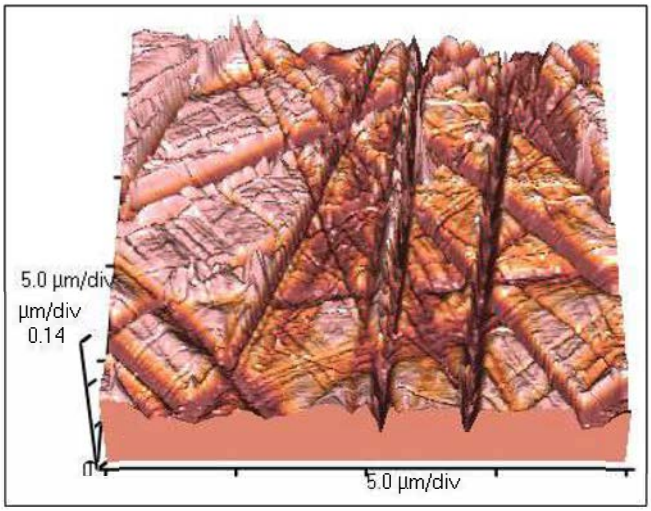

Figure 2: An AFM 3D topographic scan of the surface of a glass sample. Note that micro and nano-scale features of the glass can be observed. The dimensions of the measured image are 20 µm by 20 µm by 420 nm. (Public Domain Image)

content of the voltage in regards to the surface under study? This problem is challenging since a connection must be made between the output voltage which gives the angular deflection of the tip and the forces acting on the tip itself. In order to make this connection, it is necessary to have a reliable mathematical model of the kinematics of the cantilever.

The standard approach to this problem is a minimalist connection where, via simplifying approximations, the voltage is proportional to the force at every instant in time. This is essentially a version of *Hooke's Law* where the tip of the cantilever is treated as a simple spring with a displacement proportional to the exerted force. This model involves the underlying assumptions that the deflection at the free end is proportional to the slope there, and that the cantilever only has one degree-of-freedom, a proportionality constant. These assumptions work well for tiny deflections of the cantilever, but eventually are far too stringent for a quantitative analysis during far-from-equilibrium motion. Furthermore, this model contains a mismatch between the photodetector and the sample forces acting on the cantilever, since the instantaneous value of the slope provides only partial information about the full cantilever at that instant. This is portrayed clearly in Figure 3, where two distinct cantilever shapes, clearly resulting from different forces, produce identical output voltages. This issue becomes especially pronounced during non-equilibrium motion, and

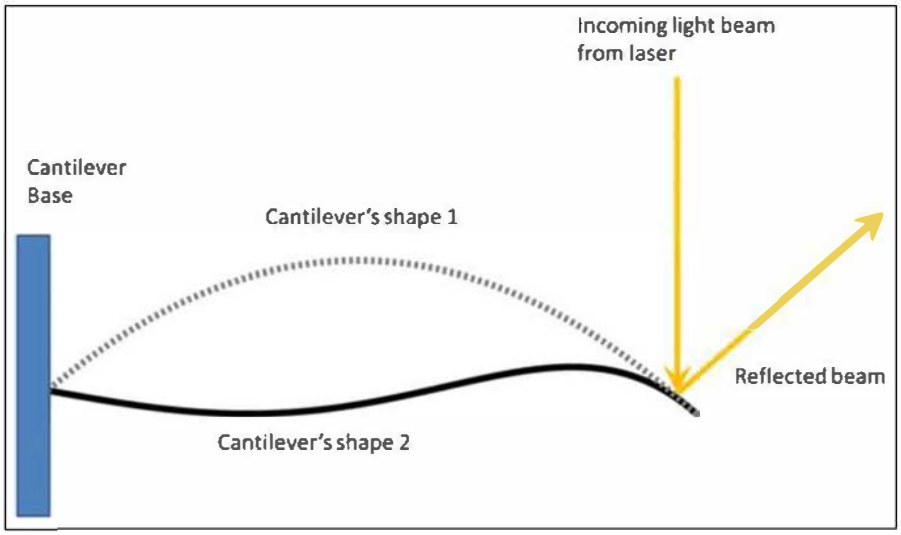

Figure 3: An incoming light ray, shown here as a vertical line, impinges the free end of the cantilever. Here the cantilever is shown to have two distinct shapes, each with the same vertical height and slope at the tip. This will produce the same voltage at the distant photodetector even though different forces are needed to produce the two shapes.[3]

demonstrates the necessity of determining full cantilever motion in order to identify forces in the sample.

A specific AFM phenomenon which causes significant issues with these linear approximations is known as *snap-to-contact*. This form of cantilever motion is a typical example of non-equilibrium motion and nonlinear external forces acting on the tip of the cantilever. It often occurs when the tip of the cantilever is brought close to the sample, where the external forces cause it to "snap" down onto the surface. An example of the voltage data obtained from this event is shown in Figure 4. Snap-to-contact has the specific advantage of testing samples at closest approach, which allows for optimal sensitivity to the changing surface forces and precise lateral resolution of the sample. Thus one can see that a more accurate approach is needed to solve the inverse problem of force reconstruction from non-equilibrium tip deflection. At the turn of the century, it was shown that this approach can be found by treating the cantilever as a true extended beam that can support spatial and temporal vibrations [9].

To do this, we introduce the Euler-Bernoulli beam theory, which provides a means of calculating the deflection characteristics of a beam. Often, this theory is applied to macroscopic beams, especially in applications to mechanical engineering. However, the Euler-Bernoulli theory seems to be particularly relevant

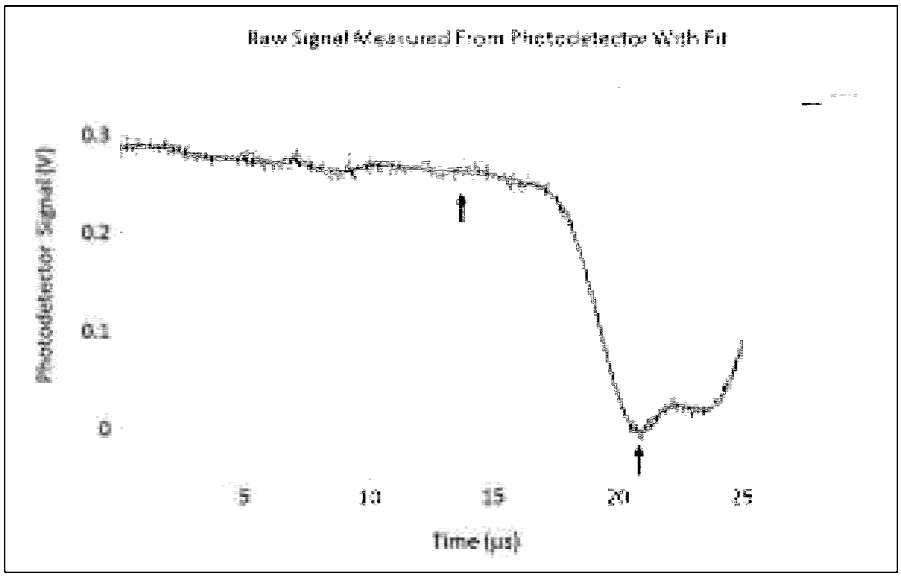

Figure 4: AFM voltage-versus-time signal measured from photodetector during snap-to-contact motion. Note that the cantilever remains in a relatively equilibrium state until the first arrow at about 15 μs where there occurs a sudden downward motion of the tip which lasts only about 5 μs until it has snapped to the surface. For reference, the first oscillation mode of an AFM cantilever is typically around 100 Hz, so this motion must correspond to significantly high frequency oscillation modes in the cantilever.[4]

to a wide range of atomic force microscopy applications because the slim cantilever's vibrations are primarily bending motions similar to that of a macroscopic flexible beam. Furthermore, the Euler-Bernoulli equation provides a rigorous connection between the complete shape of the cantilever and the force history required to produce that shape. Thus, if the shape of the cantilever can be accurately reproduced based on measurements of the tip and this agrees with experiment, one can confidently say that the forces experienced by the system can be reproduced by Euler-Bernoulli theory.

Although previous studies have been done in validating the accuracy of Euler-Bernoulli in predicting the behavior of AFM cantilever motion, these come with specific limitations. Gates and Pratt[6] used Doppler vibrometry in conjunction with Euler–Bernoulli analysis to measure the cantilever's spring constant with high accuracy. This analysis did not address either transient behavior nor the full shape of the cantilever. Payton et al[8] tackled the problem of fast imaging whereby an unknown varying force acts on the tip due to surface topography variations. While they did measure the shape of the cantilever as a function of time, the study was restricted to eigenmodes of the combined cantilever/sample system; amplitudes of the cantilever's

vibration were collected at different locations at a single frequency for times long relative to the snap-to-contact event to increase reliability. This method cannot be used in the non-equilibrium case because the snap-to-contact determines naturally and suddenly what happens to the deflection of the cantilever, so these motions are too rapid to analyze the large range of frequency eigenmodes occurring at once. Zhou, Wen and Li[10] presented a theoretical study of short cantilevers and showed how to correct the Euler–Bernoulli equation via the Timoshenko theory. Their paper did not present experimental comparison nor did it consider the full shape of the cantilever or transient behavior. Other studies contained similar limitations, primarily due to analysis of tip motion without addressing full cantilever shape, analysis of normal modes which do not account for non-equilibrium behavior, or a theoretical analysis without experimental comparison. Our work addresses these issues by solving the Euler-Bernoulli Theory for general motion of the full cantilever shape, including under non-equilibrium motion, and a comparison to experimental results.

In this thesis, we will describe a method known as *Causal Time Domain Analysis* (CTDA)[4] which provides a more robust method of deriving the full shape of the cantilever during its entire motion provided only with the voltage-versus-time trace produced by the vertical motion of the tip measured at a single cantilever location. We will describe how, using CTDA and a unique experimental setup, we can verify that the Euler-Bernoulli theory does in fact accurately reconstruct the full AFM cantilever shape, even during non-equilibrium snap-to-contact motion. This allows for the theory to be used to reconstruct surface forces from the photodetector voltage data, even in the non-equilibrium regime[3].

2 Methods

The Methods described in this paper focus on three parts: theoretical methods, experimental setup, and computational methods. We will treat the methods specifically in this order so that we may introduce the concepts in the proper order. Note that each of these three parts plays an important role in the results of this paper, since the main result of this paper is an *experimental verification of a theoretical model.* Therefore, we must first develop the theory at hand, then describe the experimental setup used to verify the theory against, and finally show the computational algorithms used to make the verification.

2.1 Theoretical Model

2.1.1 Euler-Bernoulli Model

As described in the Introduction, the goal of our paper is to verify that the motion of the AFM cantilever can be accurately described by the Euler-Bernoulli model of a flexible beam which is fixed at one end. The Euler-Bernoulli equation for a cantilevered beam is given by[7]:

$$\frac{\partial^2 u(x,t)}{\partial t^2} = -\frac{EI}{\rho A}\frac{\partial^4 u(x,t)}{\partial x^4} \tag{1}$$

where $u(x,t)$ is the deflection of the beam from equilibrium at horizontal location x along the beam and time t. E is called the elastic modulus of the cantilever material, which measures it's resistance to elastic deformation when a stress is applied to the beam. I is the area moment of inertia of the cantilever beam. ρ is the density of the cantilever material. A is the cross sectional area of the cantilever. Essentially, this equation describes the dynamics of a continuous flexible beam which may undergo various types of flexural motions and modes of oscillation, typically induced by the introduction of an external force acting on some part of the beam, here being the free end[4]. A diagram of this model is shown in Figure 5.

Note that this is a Partial Differential Equation which is fourth order in space and second order in time. This means that eventually we will need to introduce six total boundary conditions, 4 spatial boundary

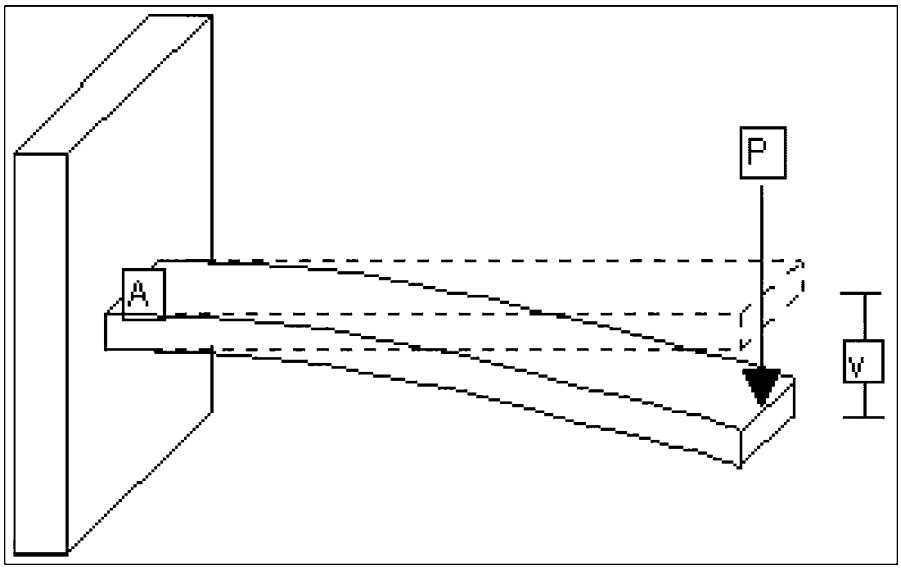

Figure 5: A diagram of a typical Euler-Bernoulli cantilever. A rectangular beam is fixed to a rigid base at one end (A) and allowed to oscillate at the free end. When a force (P) is applied to the free end of the cantilever, it undergoes oscillatory deflections (v) which are typically relatively small compared to the length of the cantilever.

conditions and 2 temporal initial conditions, in order to completely define the behavior of the cantilever. Once we have a solution for $u(x,t)$, it can be shown that we may derive the external force acting on the tip of the cantilever over time as the boundary condition:

$$F(L,t) = -AER^2 \left[\frac{\partial^3 u(x,t)}{\partial x^3}\right]_{x=L} \tag{2}$$

where R is known as the radius of gyration of the cantilever and $F(L,t)$ is the external force acting on the extreme end, $x = L$, of the cantilever. Note that Equation (2) is valid for small deflections which is the correct regime in the experiments of interest where the tip deflects well below 0.1 µm, while the cantilever length is in the 100 µm range[4]. Although Equation (2) is the fundamental aspect of the Euler Bernoulli model which allows for the reconstruction of forces acting on the cantilever, the focus of this paper will instead be on Equation (1) since our primary goal is to verify that this model does in fact work as an accurate model of non-equilibrium cantilever motion.

2.1.2 Boundary and Initial Conditions

In order to construct a solution to Equation (1) above, we require a set of six boundary conditions specifically describing the AFM cantilever under study. We will begin by listing these boundary conditions and then explaining each one individually and the reasons why they are accurate for this problem:

Boundary Conditions:

$$u(x=0,t)=0 \tag{3a}$$

$$\left[\frac{\partial u(x,t)}{\partial x}\right]_{x=0}=0 \tag{3b}$$

$$\left[\frac{\partial^2 u(x,t)}{\partial x^2}\right]_{x=L}=0 \tag{3c}$$

$$\left[\frac{\partial u(x,t)}{\partial x}\right]_{x=L}=\frac{3\gamma V(t)}{2L} \tag{3d}$$

Initial Conditions:

$$u(x,t=0)=-\frac{\gamma V(0)}{2L^3}\left(x^3-3Lx^2\right) \tag{3e}$$

$$\left[\frac{\partial u(x,t)}{\partial t}\right]_{t=0}=-\frac{\gamma V'(0)}{2L^3}\left(x^3-3Lx^2\right) \tag{3f}$$

Equation (3a) requires that the base of the cantilever is fixed onto a solid base and thus cannot experience any deflection. Equation (3b) requires that the base of the cantilever must have a finite bend at any time and thus cannot experience any slope during the motion. Equation (3c) requires that the torque at the free end must vanish at all times and torque is proportional to the second spatial derivative of the free end. Note that this condition is necessary when dealing with classical AFM data, since this data only gives information about the slope of the cantilever at the free end, not the absolute deflection. Equation (3d) is the boundary condition which takes advantage of the AFM data and simply states that the slope of the cantilever tip at the free end is proportional, by proportionality constant γ to the voltage output, $V(t)$, of the photodetector at all times during the motion. This is justified by the nature of the AFM apparatus described in the Introduction[5].

Equations (3e) and (3f) require that the deflection of the cantilever at early times is approximately that of a cantilever at static equilibrium with no applied external forces or nonlinear motion. These conditions, along with Equation (3d), can be derived by solving the Euler-Bernoulli equation for the case of static equilibrium, as follows:

In the case of static equilibrium, the time derivatives in Equation (1) vanish,

$$\frac{\partial^4 u_s}{\partial x^4} = 0 \tag{4}$$

Integrating this equation four times with respect to x gives the result

$$u_s(x) = c_1\frac{x^3}{6} + c_2\frac{x^2}{2} + c_3 x + c_4 \tag{5}$$

Applying boundary conditions (3a-3b), we find that $c_3 = c_4 = 0$. Applying boundary condition (3c), we find that $c_2 = -c_1 L$, and thus obtain

$$u_s(x) = c_1\left(\frac{x^3}{6} - L\frac{x^2}{2}\right) \tag{6}$$

Note from Equation (6) above that $u_s(L) = -\frac{1}{3}c_1 L^3$ and $\left[\frac{\mathrm{d}u}{\mathrm{d}x}\right]_{x=L} = -c_1\frac{L^2}{2}$. Solving for c_1 in the first expression and plugging it into the second, we obtain

$$\left[\frac{\mathrm{d}u_s}{\mathrm{d}x}\right]_{x=L} = \frac{3u_s(L)}{2L} \tag{7}$$

Now, recall that the voltage data of the AFM is proportional to the slope of the tip of the cantilever. However, in the static regime for small deflections, the voltage is actually also proportional to the deflection of the tip at early times. Therefore we can substitute $u_s(L,t) = \gamma V(t)$ to obtain Equation (3d) from above:

$$\left[\frac{\mathrm{d}u}{\mathrm{d}x}\right]_{x=L} = \frac{3\gamma V(t)}{2L} \tag{8}$$

Note that since the voltage is proportional to the slope at the extreme end, this relationship is applicable even in the dynamic regime. Thus we have verified Equation (3d). In order to verify Equations (3e-3f), simply

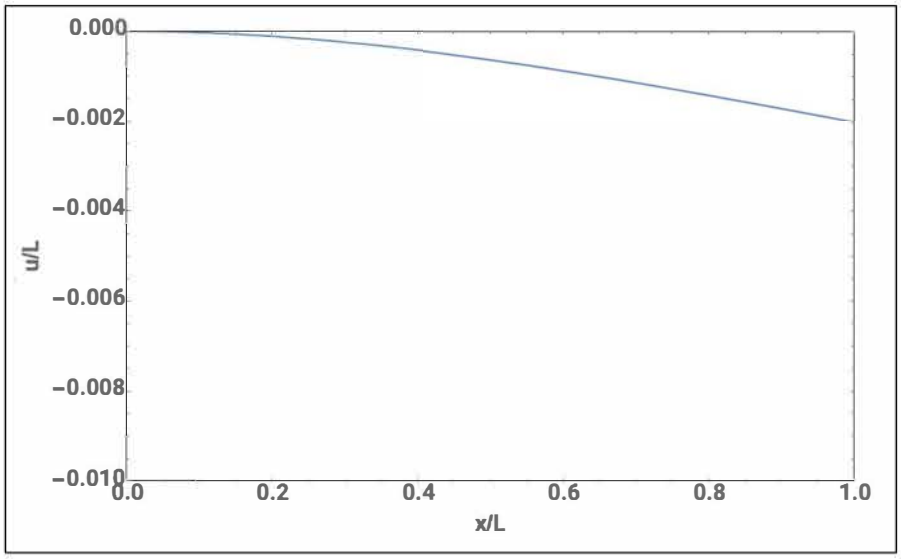

Figure 6: A plot of a typical initial condition generated by the static solution of Equation (9). Note that the magnitude of the deflection is much smaller than the full length of the cantilever, as expected for equilibrium motion.

recall that $\left[\frac{\mathrm{d}u}{\mathrm{d}x}\right]_{x=L} = -c_1\frac{L^2}{2}$ and so with Equation (8), it is clear that at early times during equilibrium motion $c_1 = -\frac{3\gamma V(0)}{L^3}$. Plugging all of the coefficients back into Equation (5) gives

$$u_s(x) = -\frac{\gamma V(0)}{2L^3}\left(x^3 - 3Lx^2\right) \tag{9}$$

This result, along with its time derivative, thus verifies the conditions in Equations (3e) and (3f). An example plot of the typical shape of the static equilibrium initial condition is shown in Figure 6.

Thus we have verified the proper boundary and initial conditions that are required to reproduce cantilever shape from the Voltage data at the tip of the cantilever. However, as is clear from the nature of real AFM cantilever data, with motion at the micrometer scale, we must normalize the data in order to deal with it computationally.

2.1.3 Introduction of Dimensionless Factors

In order to properly translate the PDE in Equation (1) and the conditions of Equation (3) into a computational model, we must adimensionalize these equations to avoid numerical issues with extremely small numerical results. Doing this requires the introduction of various physical constants which characterize the

specific cantilever of study. This allows the problem to be generalized to a cantilever with arbitrary physical parameters, solved computationally, and then the physical parameters subsequently reinserted.

First, note that we may simplify the original PDE in Equation (1) in such a way that will remove the complex quantities which represent various physical characteristics of the cantilever. This is simply done by measuring both the length, L, and the first resonance frequency, ω, of the actual cantilever. The value of ω can be obtained easily through experiment. Most commercial AFMs have the capability to obtain this value using a *thermal tune*, where thermal noise knocks the cantilever into its resonant modes. The first amplitude peak in the frequency-space is easy to spot, and represents the first resonant frequency.

By analysis of the resonance modes of the Euler-Bernoulli equation, one will obtain the relation,

$$\frac{\rho A L^4 \omega^2}{EI} = (1.8751)^4 \equiv \phi \tag{10}$$

where ρ, A, E, and I are the same physical parameters described in Equation (1). ω is the first resonance frequency of the cantilever, and L is the horizontal length of the cantilever from base to tip. This simplifies the Euler-Bernoulli PDE to

$$\frac{\partial^2 u(x,t)}{\partial t^2} = -\frac{L^4 \omega^2}{\phi} \frac{\partial^4 u(x,t)}{\partial x^4} \tag{11}$$

From here, we may adimensionalize the variables under study, specifically u and x, with dimensions of length, and t with dimensions of time. The natural way of introducing dimensionless parameters is

$$y = \frac{u}{L} \tag{12a}$$

$$\xi = \frac{x}{L} \tag{12b}$$

$$\tau = \omega t \tag{12c}$$

From here, we may substitute the dimensionless quantities into the Euler-Bernoulli equation and rearrange to obtain,

$$\phi \frac{\partial^2 y}{\partial \tau^2} = -\frac{\partial^4 y}{\partial \xi^4} \tag{13}$$

We use a similar analysis to adimensionalize the boundary and initial conditions, with an added parameter given by $\tilde{\gamma} = \gamma/L$, to obtain Boundary Conditions:

$$y(\xi = 0, \tau) = 0 \tag{14a}$$

$$\left[\frac{\partial y(\xi,\tau)}{\partial \xi}\right]_{\xi=0} = 0 \tag{14b}$$

$$\left[\frac{\partial^2 y(\xi,\tau)}{\partial \xi^2}\right]_{\xi=1} = 0 \tag{14c}$$

$$\left[\frac{\partial y(\xi,\tau)}{\partial \xi}\right]_{\xi=1} = \frac{3}{2}\tilde{\gamma}V(t) \tag{14d}$$

Initial Conditions:

$$y(\xi, \tau = 0) = -\frac{1}{2}\tilde{\gamma}V(0)\left(\xi^3 - 3\xi^2\right) \tag{14e}$$

$$\left[\frac{\partial y(\xi,\tau)}{\partial \tau}\right]_{\tau=0} = -\frac{1}{2}\tilde{\gamma}V'(0)\left(\xi^3 - 3\xi^2\right) \tag{14f}$$

Equipped with these fully adimensionalized Euler-Bernoulli PDE, Equation (13), and boundary and initial conditions, Equation (14), we may construct an algorithm to solve this problem for given AFM voltage data and verify that it in fact matches experimental results.

2.2 Experimental Setup

Returning to the physical problem of the AFM microscope and its construction, we are faced with a problem when attempting to verify the Euler-Bernoulli analysis given above. The experiment we would like to perform is in the form of displacement versus time measurements for many points along the long axis of the cantilever. By contrast, conventional data collection in Atomic Force Microscopy is at a single point, typically near the hanging end of the cantilever. We solved this problem by working with a team who had constructed a unique AFM specifically designed to measure the deflection of the cantilever at various points along the length of the cantilever. This AFM used an apparatus known as *Laser Doppler Vibrometry.*

2.2.1 Laser Doppler Vibrometry

A schematic of the Laser Doppler Vibrometry equipment used in this specific AFM is shown in Figure 7. A vibrometer was attached to a cantilever mount at 12.5°. By measuring the Doppler shift in light frequency between the emitted wave and the returning wave, the velocity of the cantilever in the direction perpendicular to the lever's surface could be recorded with high bandwidth (up to 20 MHz). The sample material (a piece of freshly cleaved mica) was cycled sinusoidally toward and away from the cantilever tip (Bruker MSNL lever B, 200 µm long rectangular SI_3N_4 cantilever with a spring constant of $0.02\,\mathrm{N\,m^{-1}}$, a thermal tune measured first mode resonance, $\omega = 14.65\,\mathrm{kHz}$, and a pyramidal tip) using a piezo stage with closed loop capacitance control at 50 Hz with an amplitude of $(850.0 \pm 0.1)\,\mathrm{nm}$ (maximum velocity was therefore $267\,\mu\mathrm{m\,s^{-1}}$). The data obtained was collected at the point in the motion of the stage with the sample moving towards the cantilever tip at a velocity of $(150 \pm 7)\,\mu\mathrm{m\,s^{-1}}$. Z-motion monitoring was done along the cantilever at approximately every 1 µm while the cantilever underwent multiple snaps-to-contact. Note that this means that each experimental plot of displacement-vs-time was performed during a different snap and thus the individual snaps may not have occurred at the same measured moment in time.

2.2.2 Experimental Data Analysis

Once the experimental data was obtained from the Laser Doppler Vibrometry experiment, a certain amount of computational analysis was required in order to reliably use this data as a boundary condition in the Euler Bernoulli algorithm, as well as ensuring that the data could be used as a proper experimental comparison to the theoretical results which would be obtained.

We began with a data set containing approximately 200 displacement-time traces of the cantilever motion towards the sample. These 200 points were taken at various locations along the cantilever, spanning from the tip (labeled x_1 in Figure 7), to the base of the cantilever (labeled x_{210} in Figure 7). Each point demonstrated a snap-to-contact event which occurs for about 25 µs. First, a small subset of these traces had to be removed

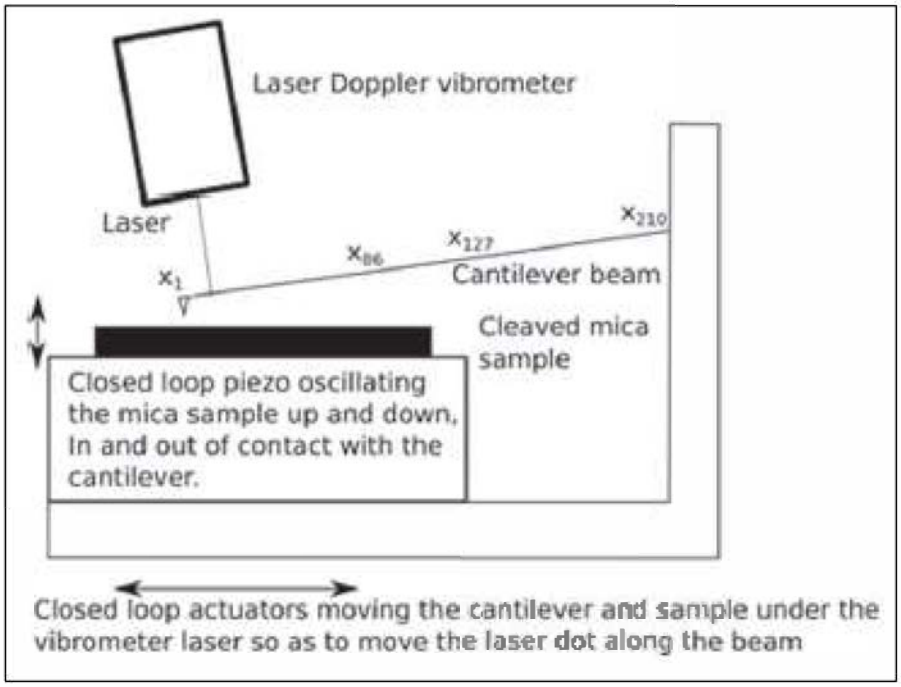

Figure 7: Diagram of the Laser Vibrometry setup used to experimentally measure cantilever deflections during the snap-to-contact. The cantilever is shown with indices along the long axis of the cantilever each separated by about 1 µm.

due to experimental issues resulting in chaotic, unrecognizable data. However, since very few points were removed relative to the total 210 points along the cantilever, this did not severely affect the final analysis of the cantilever motion. Additionally, to ensure that the input to our model matched the initial conditions of the theory we used, it was necessary to have no displacement at early times corresponding to a motionless cantilever when the tip and sample are well separated and not interacting. To achieve this, we found the average displacement value prior to the snap, and then used the collected data to find the last time the recorded data achieved this value prior to entering the snap-in region. We then appended a range of identical values of this average to the start of each snap thus guaranteeing a well-behaved input.

Next, we noticed that since the Laser Doppler Vibrometry was performed individually for each point along the length of the cantilever beam, the snap-to-contact events appeared out of phase with eachother. This occured since each individual snap-to-contact event may have began at different moments after the data began recording. Thus it was necessary to shift the individual snaps so they were in-phase with each

other. This was done by cross-correlating the data streams over a short time period that spanned the snap-to-contact. In other words, by assuming that adjacent points along the length of the cantilever will approximately begin to descend at the same time, we could cross-correlate the displacement-time traces at all adjacent points to determine the proper phase shifts.

Next, we observed a significant amount of external noise in the experimental data for each displacement-time trace. An example plot of a displacement-time trace for a point about 15 µm from the tip of the cantilever is shown in Figure 8. Apparent in the typical snap-to-contact event shown, there are a few plateaus in the traverse of the cantilever toward the surface. In some cases, the path of the lever even seems to reverse direction for a short time before continuing on down. It is possible that high frequency oscillations of the cantilever due to the thermal bath or some other source existed as the state of the lever prior to its entering the snap-to-contact regime. Conventional cantilever analysis would treat these as higher order normal modes. However, the amplitude, frequency, and phase of such modes all depend intimately on the boundary conditions at the hanging end of the cantilever. During snap-to-contact, this boundary is changing so rapidly that the lever is unable to move through a complete period of an oscillation before the boundary condition has substantially changed because the tip is now closer to the surface. Thus, the concept of a mode is not well defined during the snap-to-contact event, as explained in the Introduction. In an attempt to determine what range of frequencies the cantilever used would go through as it traversed the snap-to-contact, we solved for the normal modes of this cantilever. In going from large separation to contact: the first free mode of the lever goes from 0 kHz to 15 kHz, the second free mode goes from 75 kHz to 95 kHz, and the third free mode goes from 253 kHz to 266 kHz. None of these ranges includes the observed oscillation frequency near 200 kHz seen in our data. This makes it unlikely that these oscillations are a reflection of higher order resonances in the lever. Thus we concluded that these short time events came from some electronic source related to the Doppler system used to measure the cantilever displacements.

Since we had determined that this noise in the data was due to external sources, we decided to focus on

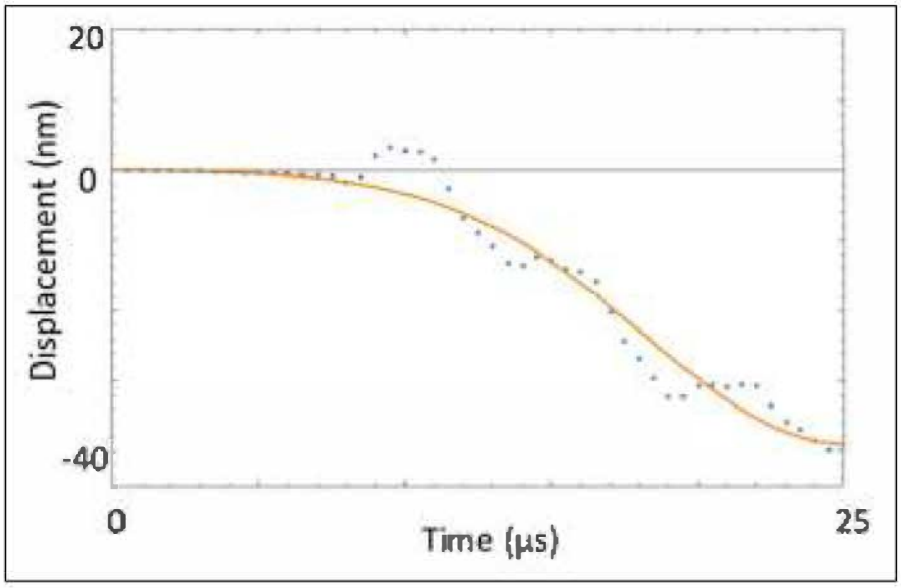

Figure 8: Snap-to-contact displacement of a point about 15µm from the free end of the cantilever as a function of time. Also shown is a best fit EVE curve that helps the eye follow the general trend and is useful in matching the phases of multiple data sets like the one shown.

the main feature of the monotonic descent of the cantilever towards the sample surface. In order to extract this specific feature from the data, we used a model known as the *EVE Model*[2], which is defined by the equation,

$$V(t) = V_0 - Ae^{-\alpha(t-t_1)^2} \tag{15}$$

where V_0 is the voltage before the snap-to-contact, A is the voltage drop, t_1 is the time to maximum voltage drop, t is time, and the parameter α controls the snap-to-contact span time. Although this model is typically used for smoothing out experimental voltage-time traces for classical AFMs, we observed that

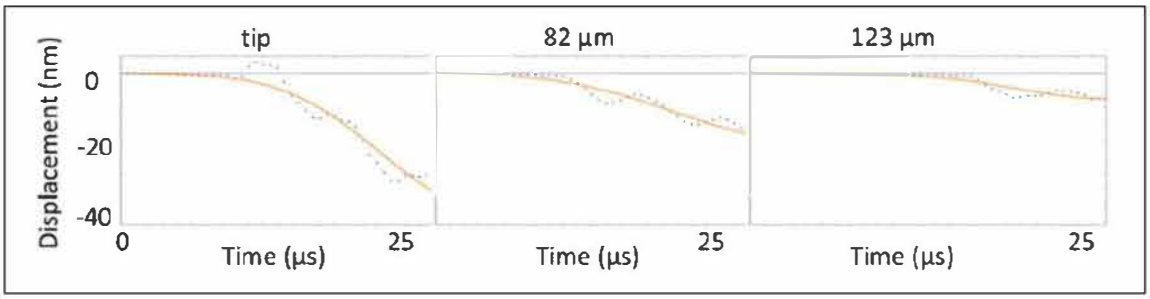

Figure 9: Displacement versus time curves for three locations along the lever: at the tip, 82µm back from the tip, and 123µm back from the tip. The blue dots are the original noisy experimental data and orange curve is EVE fit.

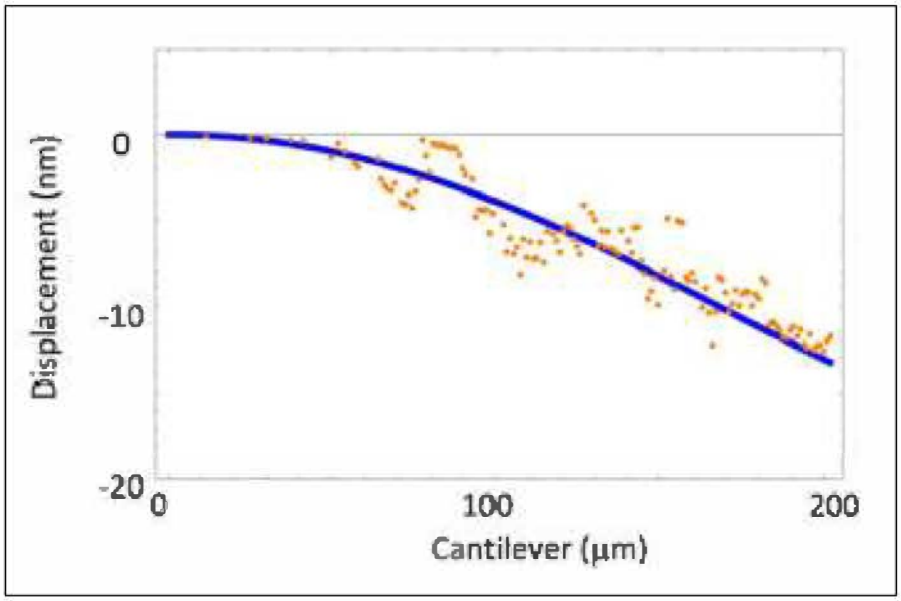

Figure 10: Instantaneous positions of monitored experimental points along the cantilever are shown 15 μs after the start of the snap-to-contact. The blue trend line represents the real cantilever.

the displacement-time traces generated by the Laser Doppler Vibrometry displayed a similar behavior and this model could be used to isolate the specific snap-to-contact behavior which we aimed to study. Plots of several displacement-time curves along the length of the cantilever are shown in Figure(9) with their EVE fits.

Once we had compiled all of these fixes and smoothing to the experimental data, we could construct a plot of the experimental motion of the cantilever over time, as shown in Figure 10. Note that the general trend of the experimental points already demonstrates the behavior of the full cantilever during the snap-to-contact motion.

Finally, before we could verify that this experimental data indeed matches the results of our theory, it was necessary to make certain changes to the boundary conditions of our theoretical model in order to account for the difference in the nature of the input data. Note that the original boundary conditions in Equations (3) and (14) were designed for a classical AFM, which generates voltage-time traces describing the *slope* of the cantilever tip during its motion on the sample. However, the experimental data from the Laser Doppler Vibrometry apparatus generates displacement-time traces describing the *displacement* of points along the

cantilever during its motion. In order to reconcile this difference in our theory, it was necessary to make changes to the boundary conditions (14c-14d), as well as the initial conditions (14e-14f).

First, we replaced the boundary conditions (14c) and (14d). Recall that the first of these requires that there is no torque applied to the tip of the cantilever during its motion and the second requires that the slope of the cantilever tip is proportional to the voltage at all times. However, since we now directly have data about the displacement of the tip at all times, call this $f(t)$ and the slope of the tip at all times, call this $s(t)$, we can change these boundary conditions to simply state,

$$y(\xi = 1, \tau) = f(\tau) \tag{16a}$$

$$\left[\frac{\partial y(\xi, \tau)}{\partial \xi}\right]_{\xi=1} = s(\tau) \tag{16b}$$

where $f(\tau)$ and $s(\tau)$ are dimensionless functions obtained from the experimental data at the tip of the cantilever. To generate these functions, we simply took the last 5 points of the experimental data near the tip and calculated the average displacement, $f(t)$, and the average slope, $s(t)$. By scaling these functions in time, we obtain the proper functions $f(\tau)$ and $s(\tau)$ to use as boundary conditions for the tip displacement and slope, respectively.

The initial conditions (14e) and (14f) were also replaced in a similar manner. By solving the equilibrium equation in a similar way to equations (4-9), requiring that $u(L) = f(t = 0)$ and $\left[\frac{\mathrm{d}u}{\mathrm{d}x}\right]_{x=L} = s(t = 0)$, and then adimensionalizing all of these parameters, we obtained the new initial conditions,

$$y(\xi, \tau = 0) = (s(0) - 2f(0))\xi^3 + (3f(0) - s(0))\xi^2 \tag{17a}$$

$$\left[\frac{\mathrm{d}y}{\mathrm{d}\tau}\right]_{\tau=0} = (s'(0) - 2f'(0))\xi^3 + (3f'(0) - s'(0))\xi^2 \tag{17b}$$

Finally, with all of the theory constructed with the proper initial conditions, and the experimental data properly prepared, we could use an algorithm to verify that our theoretical model does in fact match the obtained experimental results. The process of this algorithm will be described in the next section.

2.3 Computational Methods

Here we describe the algorithm used to solve the Euler-Bernoulli theory with the given boundary conditions. This algorithm was constructed based upon a method known as *Causal Time Domain Analysis* (CTDA). This is known to be a more robust method for converting the voltage-versus-time trace, or in this case displacement-versus-time trace, produced by the vertical motion of the tip measured at a single cantilever location into data for the motion of the entire cantilever motion over time.

The CTDA algorithm is essentially a finite-element method which discretizes the spatial and temporal variables of the solution. This transforms our inverse problem of solving a Partial Differential Equation into a linearized Matrix equation which can then be solved by matrix inversion.

We begin by taking the spatial variable ξ and the temporal variable τ and and treating their domain of interest as a mesh rather than a continuous space. The variable ξ will be represented by the array of values from $\xi = 0$ to $\xi = 1$ spaced evenly by a spacing given by $\Delta\xi = 1/N$ where N gives the number of sample points in the spacing. In other words, we model the full length of the beam as a set of discrete points along the length of the beam rather than a continuous beam. An advantage to this approach is that the given experimental data is also discretized along the length of the beam, thus allowing for an easier comparison of point to point. The time variable τ will also be discretized with a uniform spacing $\Delta\tau$, however since we may determine the motion of the cantilever arbitrarily far in the future, we may avoid assigning a fixed number of sample points along the time axis. A 3D rendered demonstration of this method is included in Figure 11.

We begin by giving the general definition of a finite element method with the calculus of finite differences. In methods of these types, functions of two variables such as $y(\xi, \tau)$ become two dimensional arrays represented by a pair of indices. Thus, we define the spatial index n such that $n = 0, 1, 2, ..., N$ along the length of the cantilever. Note that $n = 0$ represents the cantilever base and $n = N$ represents the cantilever tip. The temporal index m is defined such that $m = 0, 1, 2, ...$ and represents the evolution of the motion

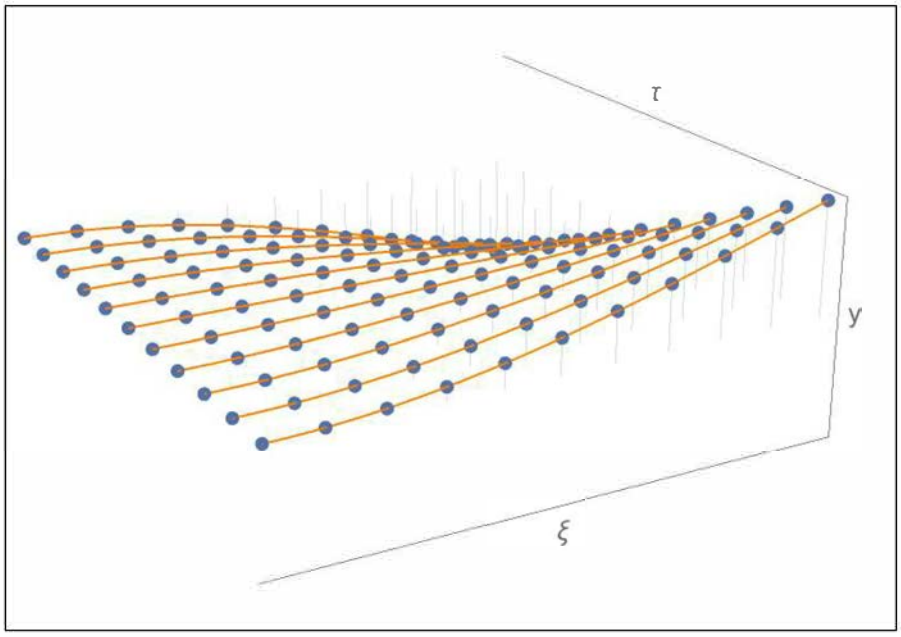

Figure 11: A 3D demonstration of the finite element method used in CTDA. Note that the blue points represent the various values of y along both spatial and time dimensions. The orange lines represent the cantilever shape at a given time. Here, time is represented as a spatial dimension and we can view the full dynamics of the cantilever as a mesh of points in 3D space.

of the cantilever with time. Note that $m = 0$ represents the initial time $\tau = 0$ and each subsequent index represents later times spaced evenly by $\Delta\tau$. We may then define the function $y(\xi, \tau)$ and its finite partial derivatives in the CTDA form as follows:

$$y(\xi, \tau) \quad \rightarrow \quad y_{n,m} \tag{18a}$$

$$\frac{\partial y}{\partial \xi} \quad \rightarrow \quad \frac{\Delta y}{\Delta \xi} = \frac{y_{n+1,m} - y_{n,m}}{\Delta \xi} \tag{18b}$$

$$\frac{\partial^2 y}{\partial \xi^2} \quad \rightarrow \quad \frac{\Delta^2 y}{\Delta \xi^2} = \frac{y_{n+1,m} - 2y_{n,m} + y_{n-1,m}}{\Delta \xi^2} \tag{18c}$$

$$\frac{\partial^4 y}{\partial \xi^4} \quad \rightarrow \quad \frac{\Delta^4 y}{\Delta \xi^4} = \frac{y_{n+2,m} - 4y_{n+1,m} + 6y_{n,m} - 4y_{n-1,m} + y_{n-2,m}}{\Delta \xi^4} \tag{18d}$$

Note that the partial difference expressions defined above also apply to the τ temporal variable, where the index shifts apply to the m index instead of n.

Using these finite differences, we can convert the Euler-Bernoulli equation given by Equation (13) into

finite element form:

$$\phi\left(\frac{y_{n,m+1}-2y_{n,m}+y_{n,m-1}}{\Delta\tau^2}\right)=-\left(\frac{y_{n+2,m}-4y_{n+1,m}+6y_{n,m}-4y_{n-1,m}+y_{n-2,m}}{\Delta\xi^4}\right) \tag{19}$$

Here we define the dimensionless coefficient $\Lambda=\frac{\Delta\tau^2}{\phi\Delta\xi^4}$ and rearrange the equation to obtain

$$(y_{n,m}-2y_{n,m-1}+y_{n,m-2})=-\Lambda\left(y_{n+2,m}-4y_{n+1,m}+6y_{n,m}-4y_{n-1,m}+y_{n-2,m}\right) \tag{20}$$

Here, Equation (20) represents the CTDA form of the Euler-Bernoulli equation to be used in our algorithm. To complete the analysis, we must also discretize the boundary conditions as follows:

$$y_{0,m}=0 \tag{21a}$$

$$\frac{y_{1,m}-y_{0,m}}{\Delta\xi}=0 \tag{21b}$$

$$y_{N,m}=f_m \tag{21c}$$

$$\frac{y_{N,m}-y_{N-1,m}}{\Delta\xi}=s_m \tag{21d}$$

Note here that the above equations are simply the same boundary conditions as Equations (14a-14b) and (16a-16b), with the finite element method introduced. The arrays given by f_m and s_m are simply the discrete counterparts of the functions $f(\tau)$ and $s(\tau)$, where the two functions are sampled at discrete points spaced by $\Delta\tau$.

From Equations (21a) and (21b), it can be simply derived that $y_{0,m}=y_{1,m}=0$. The last two boundary conditions (21c) and (21d) can be simplified to the two conditions,

$$y_{N,m}=f_m \tag{22a}$$

$$y_{N-1,m}=f_m-s_m\Delta\xi \tag{22b}$$

thus giving us the full behavior of the cantilever at both the base and tip at all times, which acts as the natural discrete counterpart to the continuous boundary conditions expressed earlier.

Now that we have a full solution for the cantilever at both the tip and the base for all times, we can use the Euler-Bernoulli expression derived in Equation (20) along with the initial conditions to find the full shape

of the cantilever at all times. Returning now to Equation (20), we rearrange in order to find an expression for the cantilever at a time index m given the two previous time indices $m-1$ and $m-2$,

$$\Lambda y_{n+2,m} - 4\Lambda y_{n+1,m} + (6\Lambda + 1)\, y_{n,m} - 4\Lambda y_{n-1,m} + \Lambda y_{n-2,m} = 2y_{n,m-1} - y_{n,m-2} \tag{23}$$

We may observe the behavior of this equation for various points along the length of the cantilever. For example, letting $n = 2$ and using the proper boundary conditions from Equation (21) gives

$$\Lambda y_{4,m} - 4\Lambda y_{3,m} + (6\Lambda + 1)\, y_{2,m} = 2y_{2,m-1} - y_{2,m-2} \tag{24}$$

This equation relates the value of the point at $n = 2$ at two previous times, $m-1$ and $m-2$, to determine the value of points at $n = 2, 3, 4$ at time m. Similarly for $n = 3$, we obtain

$$\Lambda y_{5,m} - 4\Lambda y_{4,m} + (6\Lambda + 1)\, y_{3,m} - 4\Lambda y_{2,m} = 2y_{3,m-1} - y_{3,m-2} \tag{25}$$

Clearly this pattern continues until the final point along the beam at $n = N-2$, since the points at $n = N-1$ and $n = N$ are already fully determined by boundary conditions. For $n = N-2$, we obtain

$$(6\Lambda + 1)\, y_{N-2,m} - 4\Lambda y_{N-3,m} + \Lambda y_{N-4,m} = 2y_{N-2,m-1} - y_{N-2,m-2} - 3\Lambda f_m - 4\Lambda s_m \Delta\xi \tag{26}$$

Notice that instead of $y_{N-1,m}$ or $y_{N,m}$ terms, these were replaced by the result of the boundary conditions in Equation (22) and moved to the other side since they are independent of n. From here, we obtain a total of $N-2$ coupled linear equations which relate the shape of the cantilever at previous time points to the

shape at time m. This set of equations can be represented by the matrix equation,

$$\begin{pmatrix} 1+6\Lambda & -4\Lambda & \Lambda & 0 & 0 & 0 & \cdots & & & & & & \\ -4\Lambda & 1+6\Lambda & -4\Lambda & \Lambda & 0 & 0 & \cdots & & & & & & \\ \Lambda & -4\Lambda & 1+6\Lambda & -4\Lambda & \Lambda & 0 & \cdots & & & & & & \\ 0 & \Lambda & -4\Lambda & 1+6\Lambda & -4\Lambda & \Lambda & \cdots & & & & & & \\ \vdots & \vdots & \vdots & \vdots & \vdots & \vdots & \ddots & \vdots & \vdots & \vdots & \vdots & \vdots & \vdots \\ & & & & & & \cdots & 0 & 0 & \Lambda & -4\Lambda & 1+6\Lambda & -4\Lambda \\ & & & & & & \cdots & 0 & 0 & 0 & \Lambda & -4\Lambda & 1+6\Lambda \end{pmatrix} \begin{pmatrix} y_{2,m} \\ y_{3,m} \\ y_{4,m} \\ y_{5,m} \\ \vdots \\ y_{N-3,m} \\ y_{N-2,m} \end{pmatrix}$$

$$= \begin{pmatrix} 2y_{2,m-1} - y_{2,m-2} \\ 2y_{3,m-1} - y_{3,m-2} \\ 2y_{4,m-1} - y_{4,m-2} \\ 2y_{5,m-1} - y_{5,m-2} \\ \vdots \\ 2y_{N-3,m-1} - y_{N-3,m-2} - \Lambda f_m - \Lambda s_m \Delta\xi \\ 2y_{N-2,m-1} - y_{N-2,m-2} - 3\Lambda f_m - 4\Lambda s_m \Delta\xi \end{pmatrix} \quad (27)$$

where the last two entries in the resultant vector have added terms due to the boundary conditions given by Equation (22). It can be easily verified that the matrix equation above contains every equation that can be derived from Equation (23) by plugging in $n = 2, 3, 4, ..., N-2$.

Clearly, once we have the system written in this form, $\mathbf{A} \cdot \vec{\mathbf{y}} = \vec{\mathbf{b}}$, in order to solve for the shape of the full cantilever at a given time m, knowing the shape at times $m-1$ and $m-2$, we simply invert the matrix $\mathbf{A}$ above. Preforming this matrix inversion at each time step allows us to completely reconstruct the shape of the cantilever at any time starting from the initial conditions described in Equation (17), simply by multiplying by the inverse matrix to find $\vec{\mathbf{y}} = \mathbf{A^{-1}} \cdot \vec{\mathbf{b}}$. Thus we have derived the mathematical foundation of the Causal Time Domain Analysis algorithm to fully reconstruct the full shape of the cantilever given any boundary conditions specifying the motion of only the tip of the cantilever throughout its motion.

3 Results

Summarizing the methodology of the previous section, we performed the following process to compare the Euler-Bernoulli Theory to the experimental Doppler Vibrometry data: We began by organizing the approximately 200 displacement-time traces obtained from the experiment which describe motion at various discrete points along the cantilever. A small number of these points which appeared to be too chaotic were deleted from the set and all points were phase shifted relative to adjacent points to ensure proper timing of the snap-to-contact event. All of these displacement-time traces were then fit to the EVE model described in Equation (15) in order to extract the general shape of the snap at each point. Next, several points at the tip of the cantilever were taken and used to determine the displacement of the cantilever tip at all times, this is called f_m, and the slope of the tip at all times, called s_m. Note that f_m was simply found by averaging the displacement-time curves of the points, and slope was found by calculating the slope of the best-fit line of the points at each time step. Equipped with f_m and s_m, we were then able to apply the Causal Time Domain Analysis algorithm to solve for the full shape of the cantilever at all times in order to compare with experiment.

Substantial measurement noise propagated from the input of our model to its output. To understand how this affected the deviation between experiment and theory, it was necessary to perform an error analysis that contained as much of the noise and its propagation through the model as possible. To do this, we took the group of points at the tip previously referred to and computed the standard deviation of both the position and slope of the tip. This population of points and their statistical properties of mean and standard deviation could be used in the analysis. This was simply done by running the CTDA algorithm three times: once on the f_m and s_m data computed from the mean position and slope of these points, once with $f_m + \sigma_{f_m}$ and $s_m + \sigma_{s_m}$, and once with $f_m - \sigma_{f_m}$ and $s_m - \sigma_{s_m}$. This allowed us to find an envelope of model shapes of the cantilever to include the error of experimental noise in the analysis.

We performed the analysis of results in two ways: First, we looked at the displacement versus time curves

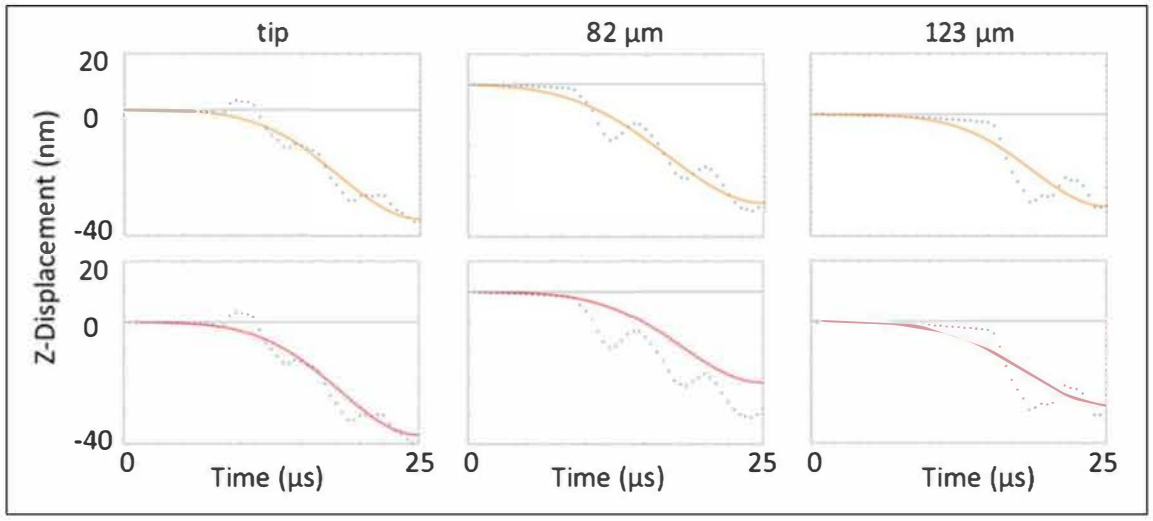

Figure 12: Comparison of experiment with theory at individual points along the long axis of the cantilever: tip (left columns), 82 µm back from tip (middle columns), 123 µm back from tip (right columns). The top row shows experimental displacement versus time curves (blue dots) along with the best fit EVE function (solid yellow line) to each curve. The bottom row shows the same experimental data but the solid red lines are the theoretical outputs from numerical solution to the Euler Bernoulli equation as described in the text.

for individual locations along the lever. Second, we looked at the entire shape of the lever at a given time point.

3.1 Analysis of Individual Displacement Vs. Time Curves

Figure 12 shows time traces at the same three points as in Figure 9 together with the theoretical outputs for comparison. The top row of curves shows these experimentally determined plots with the EVE function best fits. The lower set of curves shows the same experimental data but the solid lines represent the output from the model which used the Euler–Bernoulli solutions using data only near the end of the lever to compute the solid curves. Experiment and theory agree well at the tip (left most plots in Figure 12) which is expected since this is what was used as the input to the model. Experiment and theory also fit well 123 µm back from the end of the lever. However, the fit 82 µm back from the end is not as good. Looking carefully at noise in the system will allow us to determine if the overall motion of the cantilever is well captured by our model or not.

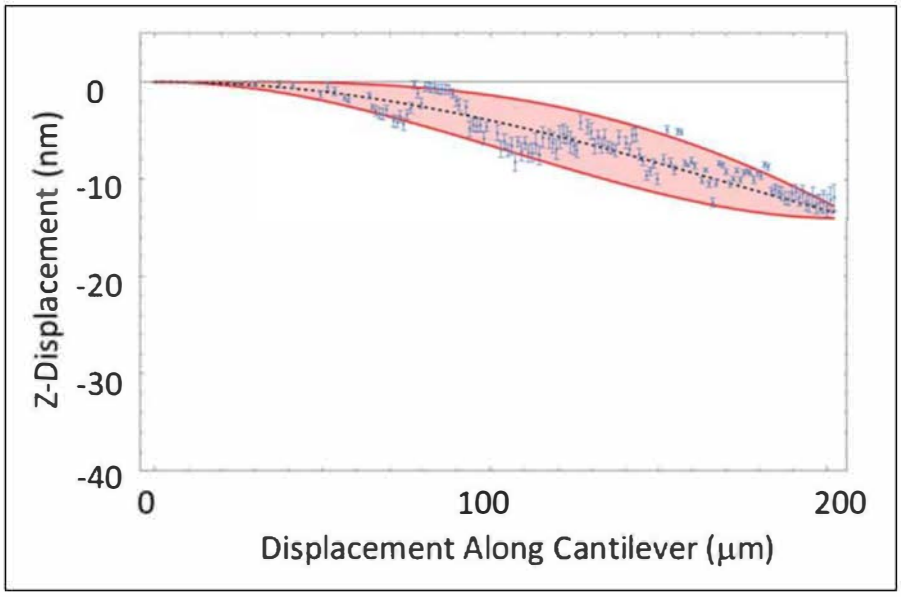

Figure 13: Snapshot of the shape of the full cantilever at an instant in time. Blue dots are the experimentally measured points. The black dotted line is the best fit to the theory. The red shaded region corresponds to the range of theoretical curves obtained using ± one standard deviation in the experimental input error to the measured slope at the end of the cantilever.

3.2 Analysis of Entire Shape of the Cantilever

Shown in Figure 13 is a snapshot of the theoretically predicted cantilever with the experimental data included. The blue points with small error bars represent the experimentally determined locations of the lever at that particular location along the long axis of the lever. The error bars were computed based on the variance of the EVE fit applied to the original experimental data at those points. Note that these errors are relatively small since the EVE curves acted as strong fits of the experimental data behavior. Note that the cantilever is represented by an envelope of model shapes rather than a single curve. The dashed black line is the algorithm model computed using the mean displacement and slope of the points at the tip. Recall that the red area was computed from the standard deviation of the noise at the tip and thus gives a representation of the contribution of noise in the data to the algorithm output. It is clear from this snapshot that the Causal Time Domain Analysis algorithm provides a strong approximation of the data obtained from the Doppler Vibrometry experiment. We may look at further snapshots to illustrate the strength of this theory more clearly.

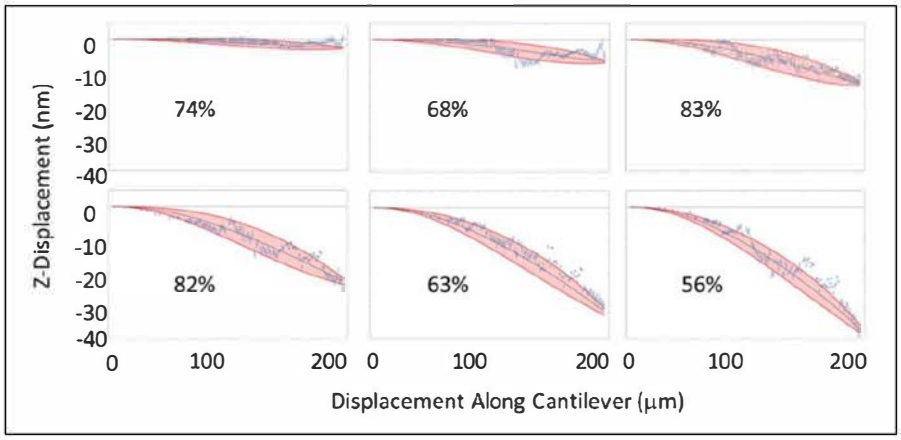

Figure 14: Snapshot of the shape of the full cantilever at an instant in time. Blue dots are the experimentally measured points. The black dotted line is the best fit to the theory. The red shaded region corresponds to the range of theoretical curves obtained using ± one standard deviation in the experimental input error to the measured slope at the end of the cantilever.

Figure 14 shows a total of six snapshots of the cantilever motion at various times throughout the snap-to-contact motion, similar to that of Figure 13. While there are some experimental points that fall outside the shaded region, it is clear that the majority of experimental points fall within the computed error. For the six typical snapshots shown in Figure 14, an average of 71% of the experimental points fall within one standard deviation of the mean. Assuming a Gaussian distribution of the experimental points about some *true mean*, the obtained distribution of experimental points about the theoretical curves is as expected.

This gives substantial evidence that the Euler–Bernoulli equation in general, and our Euler-Bernoulli model for solving the problem present when trying to convert the data provided by most commercial atomic force microscopes into known cantilever shapes, provide correct solutions.

4 Conclusions

We find that the Euler–Bernoulli theory is an appropriate framework to predict the kinematics of the cantilever during the far-from-equilibrium snap-to-contact event. We show by direct comparison with Doppler Vibrometry experiments the validity of the force-separation reconstruction algorithm based on the Euler–Bernoulli equation. Specifically, we did this comparison for the case of a cantilever undergoing far-from-equilibrium motion driven by nonlinear forces during the snap-to-contact event. The relevance of our result is that, unlike in the experiment used here, conventional atomic force microscopy experimental conditions allow collection of the slope or position versus time at only a single point on the cantilever. However, as seen in the Methods section, a distinct algorithm can be formulated to deal with this data as well.

While our rendering of the Euler–Bernoulli-based algorithm allows for the reconstruction of the full shape of the cantilever at all times, the reliability of these shapes rests ultimately on the validity of the model used. Our proof thus paves the way to use our reconstruction algorithm under conventional atomic force microscopy operating conditions. The time-consuming multiple Doppler Vibrometry measurement, while central to our test, is shown here to be no longer needed when running conventional atomic force microscopy experiments. Indeed, once one knows that Euler–Bernoulli can be used during snap-to-contact to predict the shape of the cantilever, the bending forces are readily attainable. In other words, our results should extend the ability to produce accurate force-separation curves from conventional voltage-time traces into far-from-equilibrium motion and nonlinear interactions.

Acknowledgments

I would like to acknowledge the National Science Foundation (NSF Grant No. CHE-1508085), as well as The Alexander Fund, and The Kressel Fellowship at Yeshiva University for funding this research.

I would also like to acknowledge Dr. Oliver Payton and Dr. Loren Picco at the University of Bristol for supplying the much needed Laser Doppler Vibrometry data to help us verify our theory.

I would like to thank Dr. Steven Eppell for the time he spent working with Dr. Zypman and me in analyzing the experimental data and helping with the error analysis to obtain our final results, and for his help ensuring that our final published paper made it into official publication.

Finally, I would like to thank Dr. Fredy Zypman for his time and effort working with me over the three years that we have done this research together. He helped me to become a competent physicist and taught me the importance of efficiency, collaboration, and hard work in completing fulfilling scientific research.

References

[1] G. Binnig, C. F. Quate, and Ch. Gerber. Atomic force microscope. *Phys. Rev. Lett.*, 56:930–933, Mar 1986.

[2] Steven J. Eppell, Matthew Feinstein, Li Li, Brandon White, and Fredy R. Zypman. Signal distortion in atomic force microscopy photodetector. *Review of Scientific Instruments*, 88(10), 2017.

[3] Steven J Eppell, David Friedenberg, Oliver Payton, Loren Picco, and Fredy R Zypman. Euler–bernoulli theory accurately predicts atomic force microscope cantilever shape during non-equilibrium snap-to-contact motion. *Nanotechnology*, 31(18), Feb 2020.

[4] Steven J. Eppell, Yehe Liu, and Fredy R. Zypman. Accuracy of afm force distance curves via direct solution of the euler-bernoulli equation. *AIP Advances*, 6(3), 2016.

[5] Matthew D. Feinstein. Force spectroscopy in the snap-to-contact using an atomic force microscope. Yeshiva University Honors Thesis, May 2017.

[6] Richard S Gates and Jon R Pratt. Accurate and precise calibration of AFM cantilever spring constants using laser doppler vibrometry. *Nanotechnology*, 23(37):375702, Aug 2012.

[7] Jonathan Mehlman and Fredy Zypman. Scanning probe microscope force reconstruction algorithm via time-domain analysis of cantilever bending motion. *Journal of Advanced Microscopy Research*, 9, Dec 2014.

[8] O D Payton, L Picco, M J Miles, M E Homer, and A R Champneys. Modelling oscillatory flexure modes of an atomic force microscope cantilever in contact mode whilst imaging at high speed. *Nanotechnology*, 23(26):265702, Jun 2012.

[9] Brian Todd, Steven Eppell, and Fredy Zypman. Improved analysis of the time domain response of scanning force microscope cantilevers. *Journal of Applied Physics*, 88:7321–7327, 12 2000.

[10] Xilong Zhou, Pengfei Wen, and Faxin Li. Vibration analysis of atomic force microscope cantilevers in contact resonance force microscopy using timoshenko beam model. *Acta Mechanica Solida Sinica*, 30(5):520 – 530, 2017.